AIP | Physics of Fluids

Shape of a large drop on a rough hydrophobic surface

Joonsik Park, Jaebum Park, Hyuneui Lim, and Ho-Young Kim

Citation: Phys. Fluids **25**, 022102 (2013); doi: 10.1063/1.4789494
View online: http://dx.doi.org/10.1063/1.4789494
View Table of Contents: http://pof.aip.org/resource/1/PHFLE6/v25/i2
Published by the American Institute of Physics.

PHYSICS OF FLUIDS **25**, 022102 (2013)

Shape of a large drop on a rough hydrophobic surface

Joonsik Park,[1] Jaebum Park,[2] Hyuneui Lim,[1,a)] and Ho-Young Kim[2,b)]
[1]*Department of Nature Inspired Nanoconvergence Systems, Korea Institute of Machinery and Materials, Daejeon 305-343, South Korea*
[2]*School of Mechanical and Aerospace Engineering, Seoul National University, Seoul 151-744, South Korea*

(Received 23 September 2012; accepted 8 January 2013; published online 1 February 2013)

Large drops on solid surfaces tend to flatten due to gravitational effect. Their shapes can be predicted by solving the Young-Laplace equation when their apparent contact angles are precisely given. However, for large drops sitting on rough surfaces, the apparent contact angles are often unavailable *a priori* and hard to define. Here we develop a model to predict the shape of a given volume of large drop placed on a rough hydrophobic surface using an overlapping geometry of double spheroids and the free energy minimization principle. The drop shape depends on the wetting state, thus our model can be used not only to predict the shape of a drop but also to infer the wetting state of a large drop through the comparison of theory and experiment. The experimental measurements of the shape of large water drops on various micropillar arrays agree well with the model predictions. Our theoretical model is particularly useful in predicting and controlling shapes of large drops on surfaces artificially patterned in microscopic scales, which are frequently used in microfluidics and lab-on-a-chip technology. © *2013 American Institute of Physics*. [http://dx.doi.org/10.1063/1.4789494]

I. INTRODUCTION

It is a fundamental problem in interfacial flow physics to describe the shape of a liquid drop on a solid surface. The shape of a sessile drop determines the liquid-gas and liquid-solid interfacial areas, which critically affect the rates of heat and mass transfer across the interfaces. Also the dynamics of a liquid drop impacting on a solid surface must be eventually affected by the equilibrium drop configuration. The understanding of the deformation due to external forcings such as flow-induced stresses,[1] acoustic pressure,[2] and substrate inclination[3,4] can be built based on the accurate information of the equilibrium drop shape.

For a small drop where the gravitational effect is negligible, the interior pressure of the drop is uniform thus the interface must have a uniform curvature. The pressure jump across the interface is given by the product of the surface tension coefficient and the curvature.[5,6] The length scale l at which the hydrostatic pressure $\rho g l$ is balanced by the capillary pressure γ/l is referred to as the capillary length $l_c = [\gamma/(\rho g)]^{1/2}$, where ρ and γ are the density and the surface tension of the liquid, respectively, and g is the gravitational acceleration. Therefore, a small drop whose characteristic length is much smaller than l_c can be approximated by a truncated sphere, allowing us to determine the drop shape only with the contact angle and drop volume. However, as the drop size becomes comparable to or exceeds the capillary length, the gravitational effect is no longer negligible thus the shape deviates from the truncated sphere. To obtain the shape of a liquid drop distorted by gravity, one needs to integrate the curvature related to the hydrostatic pressure by the Young-Laplace (YL) equation, which rarely allows closed-form solutions.

a)Electronic mail: helim@kimm.re.kr.
b)Electronic mail: hyk@snu.ac.kr.

There have been many attempts to obtain approximate shapes of large sessile drops. Bashforth and Adams[7] solved the YL equation including the hydrostatic effects using iterative numerical methods manually and provided the solutions in extensive numeric tables. One can predict the shape of large drops in this manner only when their volume and contact angles are known *a priori*. This model was compared with the shape of a small drop on superhydrophobic surfaces by Extrand and Moon,[8] which also provided a simplified model with some geometrical approximations. Models using a single spheroid were suggested which predicted the drop shape based on the given drop volume and apparent contact angle.[9–11] Other studies[12–14] that have either numerically or analytically found the drop profile have a common shortcoming that the contact diameter and/or the maximum diameter of the drop should be measured *a priori* in addition to the drop volume and contact angle.

Aided by the rapid advances in micro and nano-scale surface machining technology, the wetting properties of rough hydrophobic surfaces are actively studied these days. Drops on hydrophobic surfaces are more sensitive to gravitational distortion because the hydrostatic force exerted on a small area at the bottom easily dominates over the capillary force and flattens their bottom.[8] On rough hydrophobic surfaces, the mode of the solid-liquid contact plays an important role in determining the drop shape as well as the Young angle θ_Y that is given by the liquid-solid-gas combination. When the drop liquid is in intimate contact with the rough surface, it is commonly referred to as the Wenzel state.[15] When the drop is suspended on top of surface asperities, it is referred to as the Cassie-Baxter state.[16] It was recently pointed out that on solid surfaces of uneven roughness distribution, the local surface conditions immediately adjacent to the contact line determine the apparent contact angle.[17] For uniformly textured solid surfaces, however, thermodynamic analysis is able to describe macroscopic contact angles by characterizing the surface with macroscopic quantities, such as surface roughness or wetted fractions.[18,19] In particular, for very small droplets sitting on rough surfaces, which can be modeled as spherical caps due to negligible gravitational effects, minimization of the Gibbs free energy was shown to yield the apparent macroscopic contact angles exactly matching the values suggested by Wenzel and Cassie and Baxter for each wetting state.[20] This implies that one can completely describe the shape of a small drop with information of the wetting state and volume using the free energy minimization principle.

Here we aim to provide a model to predict the shape of large drops sitting on rough surfaces (hydrophobic, in particular) based on the wetting states and the free energy minimization principle. While aforementioned previous works concentrated on predicting the drop shape using a known contact angle, the model presented here does not resort to the apparent contact angle. Unlike the Young angle θ_Y valid for smooth surfaces, the apparent contact angle on rough surfaces is in many cases unavailable and difficult to define.[21] Furthermore, the apparent contact angle calculated based on the equations of Wenzel or Cassie and Baxter may differ from the angles of gravitationally flattened large drops in general. Our model can also be used to infer the wetting state of a large drop by matching the shapes that are experimentally observed and theoretically calculated by iteration. In the following, we first present a relatively simple, yet accurate model to describe the shape of a distorted large drop on hydrophobic surfaces. Considering that the flattening due to hydrostatic pressure is more severe in the lower portion of the drop than in the upper, we suggest two overlapping spheroids as a model of a drop on hydrophobic surfaces. Then, we investigate the morphology of a large drop on rough hydrophobic surfaces depending on various factors such as the drop volume, surface textures, and mode of solid-liquid contact (or wetting state), which are corroborated experimentally.

II. THEORY

The Young-Laplace equation relates the curvature of the interface to the pressure difference across the interface ΔP as

$$\gamma\left(\frac{1}{R_1}+\frac{1}{R_2}\right)=\Delta P, \tag{1}$$

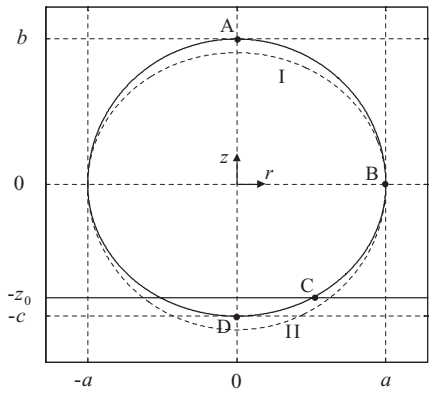

FIG. 1. The double-spheroid model of the drop contour. The upper ($z > 0$) and lower ($z < 0$) spheroid portions (solid line) are drawn by Eqs. (3) and (4), respectively. The lower spheroid is intersected by the plane $z = -z_0$. The dashed lines I and II correspond to the mirror images of the lower and upper half spheroid, respectively.

where R_1 and R_2 are the principal radii of curvature. Under a gravitational field, ΔP should account for the hydrostatic column effect, such that[22]

$$\gamma\left(\frac{1}{R_1}+\frac{1}{R_2}\right)=\frac{2\gamma}{R_0}+\frac{mg}{A_{cs}}, \tag{2}$$

where R_0 is the radius of the liquid drop at its apex where the two radii of curvature become equal, m is the mass of the liquid above a plane where the pressure is measured, and A_{cs} is the cross-sectional area of the intersecting plane. Here, we propose a drop geometry consisting of two truncated spheroids, which rigorously satisfies the YL equation at some designated boundary points, as a global approximate solution to the YL equation. In the following, we describe a procedure to determine the parameters which define the double spheroids.

Figure 1 shows the four boundary points of a model drop sitting on a hydrophobic surface, which consists of a half spheroid occupying $z > 0$ and a part of a different spheroid truncated between $z = 0$ and $z = -z_0$. The upper half spheroid with its apex at A($r = 0$, $z = b$) is a solution to

$$\frac{r^2}{a^2}+\frac{z^2}{b^2}=1 \quad (z \geq 0). \tag{3}$$

It intersects with the lower truncated spheroid described as the following at B(a, 0):

$$\frac{r^2}{a^2}+\frac{z^2}{c^2}=1 \quad (-z_0 < z \leq 0). \tag{4}$$

The lower truncated spheroid meets the solid surface at C(r_0, $-z_0$) and its extension has the bottom apex at D(0, $-c$). Since the upper and lower elliptic curves are connected at B(a, 0) where their slopes are equal, the smoothness of the drop is mathematically conserved. The combined geometry has four variables, a, b, c, and z_0. Because of the inherent nonlinearity stemming from the three-dimensional shape of a drop, two conditions—the upper elliptic approximation to the YL equation at B(a, 0) and the constant total volume equation—are used to couple the variables a with b and c with z_0. In addition, within the physically possible ranges of the two variables $b(a)$ and $c(z_0)$, the minimization of the total free energy of the drop is used to finally find the four variables.

A. Approximation for the upper spheroidal portion

In the cylindrical coordinates, the curvatures R_1^{-1} and R_2^{-1} of the spheroidal surface are respectively given by

$$\frac{1}{R_1}=\frac{z'}{r(1+z'^2)^{1/2}}=\frac{b}{(a^4-a^2r^2+b^2r^2)^{1/2}}, \tag{5}$$

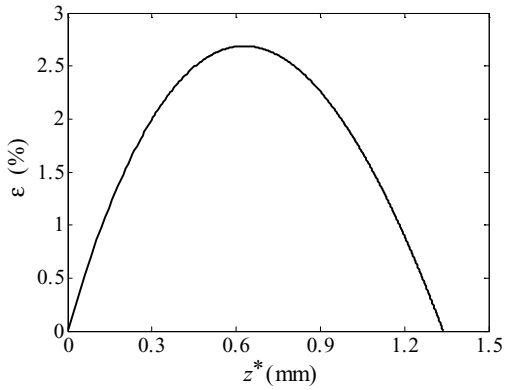

FIG. 2. The relative error of the elliptic approximation to the Young-Laplace equation for a water drop of the volume 10 μl on the substrate with the Young angle 107° and $k = 0.94$.

$$\frac{1}{R_2} = \frac{z''}{(1+z'^2)^{3/2}} = \frac{a^4 b}{(a^4 - a^2 r^2 + b^2 r^2)^{3/2}}, \tag{6}$$

where $z' = \mathrm{d}z/\mathrm{d}r$. At the drop apex A(0, b) the interface is spherical and the two radii become equal with the curvature $R_0^{-1} = b/a^2$. At the maximum radius B(a, 0) we have $R_1^{-1} = 1/a$ and $R_2^{-1} = a/b^2$. The mass m and the bottom area A_{cs} of the upper spheroid are simply $m = \frac{2}{3}\pi\rho a^2 b$ and $A_{cs} = \pi a^2$. Thus we write the YL equation at B(a, 0) as

$$\frac{a}{b^2} + \frac{1}{a} = \frac{2b}{a^2} + \frac{2}{3}\beta b, \tag{7}$$

where $\beta = \rho g/\gamma$. In this model, each point along the elliptic curve is suggested as a close approximation to the actual YL solution. In Fig. 2, we have calculated the relative error ϵ associated with this approximation. We define ϵ as the difference of the left-hand and right-hand sides of Eq. (2) normalized by the right-hand side

$$\epsilon(\%) = 100 \times \frac{\left|R_1^{-1} + R_2^{-1} - M\right|}{M}, \tag{8}$$

where $M = 2b^2/a + \beta V(z^*)/\pi/r^2(z^*)$ with z^* being the vertical distance from the apex, $r(z^*)$ the radius at z^*, $r(z^*) = a[1 - (z^*/b)^2]^{1/2}$, and $V(z^*)$ the volume of the truncated spheroid, $V(z^*) = [\pi a^2/(3b^2)](2b^3 - 3b^2 z + z^3)$. Figure 2 shows that the relative error ϵ is at most 2.7% for a drop of 10 μl in volume sitting on a rough surface with the Young angle 107° and $k = 0.94$, where k is defined below.

B. Range of *b*

It can be shown that Eq. (7), a cubic equation for a, has one real root, which gives a variable b as a function of a: $b(a)$. Here we define the range of b using the volume constraint. When the contact angle is 180°, if gravity is excluded, the drop is in a completely spherical shape having a radius $R_N = \left(\frac{3}{4\pi}V\right)^{1/3}$, where V is the drop volume. However, due to gravity, even at the contact angle of 180°, the drop sags from a spherical shape; thus $b < R_N$. Although we can proceed with this range of b, which subsequently defines the range of a via Eq. (7), it is possible to further narrow down the ranges. The volume of the full spheroid having the identical major and minor axes to those of the upper spheroid $\frac{4\pi}{3}a^2 b$ should be greater than the drop volume V. It is also evident that the volume of the upper half spheroid $\frac{2\pi}{3}a^2 b$ should be smaller than V. Combining these conditions leads to

$$\frac{3V}{4\pi a^2} < b(a) < \frac{3V}{2\pi a^2}. \tag{9}$$

C. Range of *c* and constant volume condition

We physically limit the range of c along the similar line to Sec. II B. Because the lower half spheroid sags more due to gravity than the upper half spheroid $c < b$. The volume of drop excluding the upper half spheroid $V - V_1$, where $V_1 = \frac{2}{3}\pi a^2 b$, should be smaller than the volume of the lower half spheroid $\frac{2\pi}{3}a^2 c$. Thus we have the following range of c:

$$\frac{3}{2\pi a^2}(V - V_1) < c < b. \tag{10}$$

The total drop volume $V = V_1 + V_2 - V_3$, where V_2 is the volume of the lower half spheroid and V_3 is the volume of the spheroidal cap intersected by the $z = -z_0$ plane, can now be written as

$$V = \frac{2}{3}\pi a^2 b + \frac{2}{3}\pi a^2 c - \frac{1}{3}\pi \frac{a^2}{c^2}(2c^3 - 3c^2 z_0 + z_0^3). \tag{11}$$

Given c, z_0 is calculated from the total volume constraint Eq. (11), thus the variable c can be expressed as a function of z_0: $c(z_0)$. Relations (9) and (10), at given $b(a)$, define the corresponding domain of $c(z_0)$.

D. The Gibbs free energy minimization

Now we determine the values of the parameters describing the double-spheroidal shape (a, b, c, z_0) by minimizing the total Gibbs free energy of the drop. The total Gibbs free energy is the sum of the interfacial energy of the drop area exposed to the ambient air (E_a), that of the drop bottom (E_b), and the gravitational potential energy (E_g)

$$E = E_a + E_b + E_g. \tag{12}$$

Given the drop volume V and three interfacial energies $\gamma_{lv} = \gamma$, γ_{sv}, and γ_{sl}, with the subscripts l, v, and s standing for liquid, vapor, and solid, respectively, we get $E_a = \gamma_{lv}(S_1 + S_2 - S_3)$, where S_1 is the surface area of the upper half spheroid $S(a, b, 0)$, S_2 is the surface area of the lower half spheroid $S(a, c, 0)$, and S_3 is the surface area of the lower spheroidal cap intersected by the $z = -z_0$ and $z = -c$ planes $S(a, c, z_0)$. These areas are given by the following formula:

$$S(x, y, z) = \frac{\pi}{y^2 e}\left\{y^2\left[ex^2 + y^2 \ln(exy + xy)\right] - exz\eta - y^4 \ln[exz + \eta]\right\}, \tag{13}$$

where e is the eccentricity of an ellipse, $e = [1 - (x/y)^2]^{1/2}$, and $\eta = [(exz)^2 + y^4]^{1/2}$. The interfacial energy of the drop bottom E_b is given by $E_b = \gamma_{lv}\pi r_0^2 k$, where k is a function of θ_Y and the mode of contact between liquid and solid. When the surface is in intimate contact with the rough surface (the Wenzel state), k is given by

$$k = k_W = f\frac{\gamma_{sl} - \gamma_{sv}}{\gamma_{lv}}, \tag{14}$$

where f is the surface roughness defined as the ratio of the actual area to the projected area of the solid surface. When the drop is suspended on top of surface asperities (the Cassie-Baxter state), the bottom area consists of the liquid-vapor and liquid-solid interfaces. Then we can show that

$$k = k_C = 1 + \phi\left(\frac{\gamma_{sl} - \gamma_{sv}}{\gamma_{lv}} - 1\right), \tag{15}$$

where ϕ is the wetted fraction of the solid surface. The difference of γ_{sv} and γ_{sl} is related to γ_{lv} via Young's equation: $\gamma_{sv} - \gamma_{sl} = \gamma_{lv}\cos\theta_Y$. For a drop having the shape of a truncated sphere, thermodynamic analysis reveals that $-k$ of Eqs. (14) and (15) is exactly equal to the cosine of the apparent contact angle in the Wenzel and Cassie-Baxter state, respectively, on the surfaces of uniform

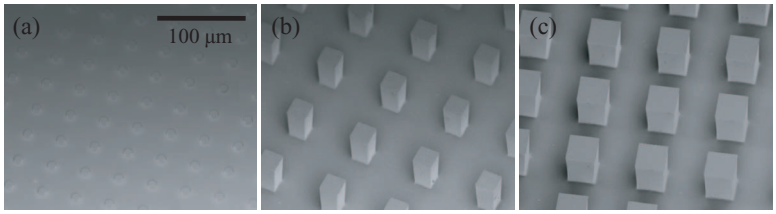

FIG. 3. Scanning electron microscopy images of the micropillars. (a) Array I; (b) array II; (c) array III.

roughness.[20] We calculate the gravitational potential energy E_g as

$$E_g = \rho g \left[V_1(h_1 + z_0) + V_{2-3}h_{2-3}\right]$$
$$= \rho g \left[\frac{2}{3}\pi a^2 b\left(\frac{3}{8}b + z_0\right) + \frac{1}{12}\pi\frac{a^2}{b^2}z_0^2\left(6c^2 - z_0^2\right)\right], \quad (16)$$

where h_1 is the z-directional distance of the center of mass of the upper half spheroid from the substrate, V_{2-3} is the volume of the truncated lower half spheroid, which is V_2 subtracted by V_3, and h_{2-3} the z-directional distance from the substrate to the center of mass of V_{2-3}.

We numerically compute the Gibbs free energies within the two-dimensional range of $b(a)$ and $c(z_0)$, then find the solution (a, b, c, z_0) corresponding to the minimum Gibbs free energy state. A rigorous mathematical proof of the uniqueness of the set (a, b, c, z_0) obtained by the foregoing procedure is yet to be established.

III. EXPERIMENTAL

We measured the shape of water drops of various volumes on solids of varying surface conditions—one flat hydrophobized silicon surface and three types of rough hydrophobized silicon surfaces. As rough hydrophobized silicon surfaces, a square array of cylindrical micropillars (array I), and two types of square arrays of square micropillars (arrays II and III) were fabricated using the deep reactive ion etching process. The dimensions of the cylindrical pillars of array I are such that $[d, h, p] = [10, 2.7, 40]$ μm, where d, h, and p are diameter, height, and pitch of the cylinders, respectively. Array I was spin-coated with 0.6% aqueous polytetrafluoroethylene (PTFE) solution at 1000 rpm for 30 s and baked at 200 °C for 30 min. The dimensions of the square pillars of array II are such that $[w, h, p] = [24, 40, 80]$ μm, where w is width of the square pillar. For array III, $[w, h, p] = [34, 40, 80]$ μm. Figure 3 shows the images of the micropillar arrays fabricated in this work. A flat silicon and arrays II and III were chemically treated with tridecafluoro-1,1,2,2-tetrahydrooctyl-trichlorosilane (FOTS).[23] We gently placed water drops with volumes ranging between 5 and 45 μl on the four kinds of horizontal surfaces. It turned out that both the arrays II and III supported the drops to result in the Cassie-Baxter state as can be checked by air layer visible between liquid and solid, Figs. 4(c) and 4(d), while such air layer is absent on the flat surface and array I, Figs. 4(a) and 4(b). To obtain the Young angle θ_Y, we measured the contact angle of small water droplets (1 mm in diameter) placed on flat surfaces treated with PTFE and FOTS, respectively, assuming the small droplets as a truncated sphere. The drop images were captured with a 0.3 mega pixel CCD camera. The drop dimensions were measured by a software and compared with theoretical predictions. All the measurements were carried out at 22 °C, which gives $\gamma_{lv} = 72.5$ mJ/m^2 and $\theta_Y = \cos^{-1}[(\gamma_{sv} - \gamma_{sl})/\gamma_{lv}] = 120°$ and 107° on the surfaces treated with PTFE and FOTS, respectively.

IV. RESULTS AND DISCUSSION

To demonstrate the minimization of the Gibbs free energy within the ranges of b and c, we show numerical calculation results of the Gibbs free energies of a 5 μl water drop on array II and a flat surface, whose results are displayed in Fig. 5. On array II, we have assumed that the drop

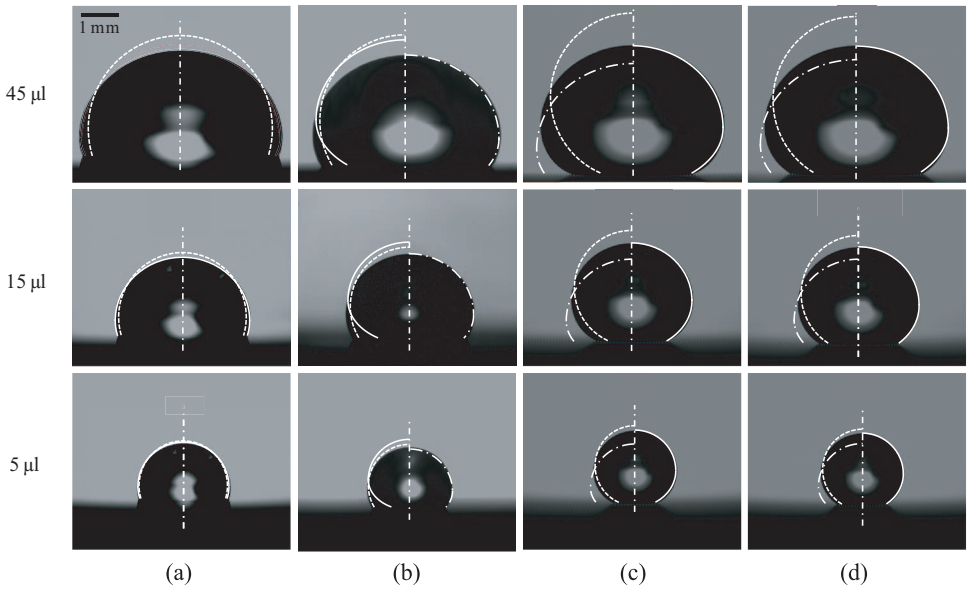

FIG. 4. Comparison of the actual drop images with theoretical models. (a) Flat surface; (b) array I; (c) array II; (d) array III. In (a), the dashed and solid lines correspond to the spherical-cap model and the double-spheroid model, respectively, In (b)–(d), the dashed line corresponds to the spherical-cap model and the dot-and-dash and solid lines correspond to the double-spheroid profiles assuming the Wenzel state and the Cassie-Baxter state, respectively.

is in the Cassie-Baxter state for which the wetted fraction of the array $\phi = 0.09$ and $k = 0.94$. The corresponding experimental image of Fig. 4(c) shows the pillars supporting the drop in the Cassie-Baxter or fakir state.[24] The flat surface hydrophobized by FOTS has $k = 0.30$ via Eq. (14) with $f = 1$. In the computation, the Gibbs free energy values are stored in a matrix whose individual elements represent a square grid of 1 μm in side length. Figure 5 shows the contour maps of the Gibbs free energies over the two-dimensional space bounded by the limits of b and c. Two solid lines indicate the range of $b(a)$ given by relation (9) and two dashed lines show the range of $c(z_0)$ given by relation (10). Because the drops of the same volume are used on the two surfaces, the areas defined by the ranges of $b(a)$ and $c(z_0)$ are equal. The location of the free-energy minimum, shown as a black dot, determines the drop shape on each surface.

In Figs. 5(a) and 5(b), the minimum point on array II is located at $b = 1.09$ mm and $c = 0.82$ mm. Because the lower and upper limits of b correspond to a complete spheroid and a half spheroid, respectively, as can be seen in relation (9), the fact that the free-energy minimum point is located close to the solid line of the lower limit of b indicates that the drop shape is nearly spherical. In relation (10), the lower and upper limits of c correspond to the contact angle of 180° and 90°, respectively. In Figs. 5(a) and 5(b), the free-energy minimum is located very close to the lower limit of c at given b, indicating that the drop must have a very high contact angle. This corresponds to the experimental measurement of the apparent contact angle 160°. Equations (7) and (11) determine the other variables $a = 1.12$ mm and $z_0 = 0.73$ mm, respectively.

For a drop on the flat surface, Figs. 5(c) and 5(d), the free-energy minimum is located at $b = 1.19$ mm, in the middle of the upper and lower limits of b. At $c = 0.77$ mm, the minimum point is rather far from the lower limits due to the relatively low contact angle. Again, we can calculate the other variables as $a = 1.23$ mm and $z_0 = 0.28$ mm.

Our contour map of the Gibbs free energy provides information beyond the shape of the minimum energy state. In Figs. 5(a) and 5(b), the free-energy minimum point on the superhydrophobic array II is surrounded by the steep downslopes of energy values. Since the gradients toward the minimum point are large, the variations of the drop profile and of the contact angle near the equilibrium due to external disturbances are expected to be small. On the other hand, the free-energy minimum point on the flat hydrophobic surface in Figs. 5(c) and 5(d) is approached by mild downslopes. This suggests that the drop shape and contact angle are more likely to vary due to small perturbations

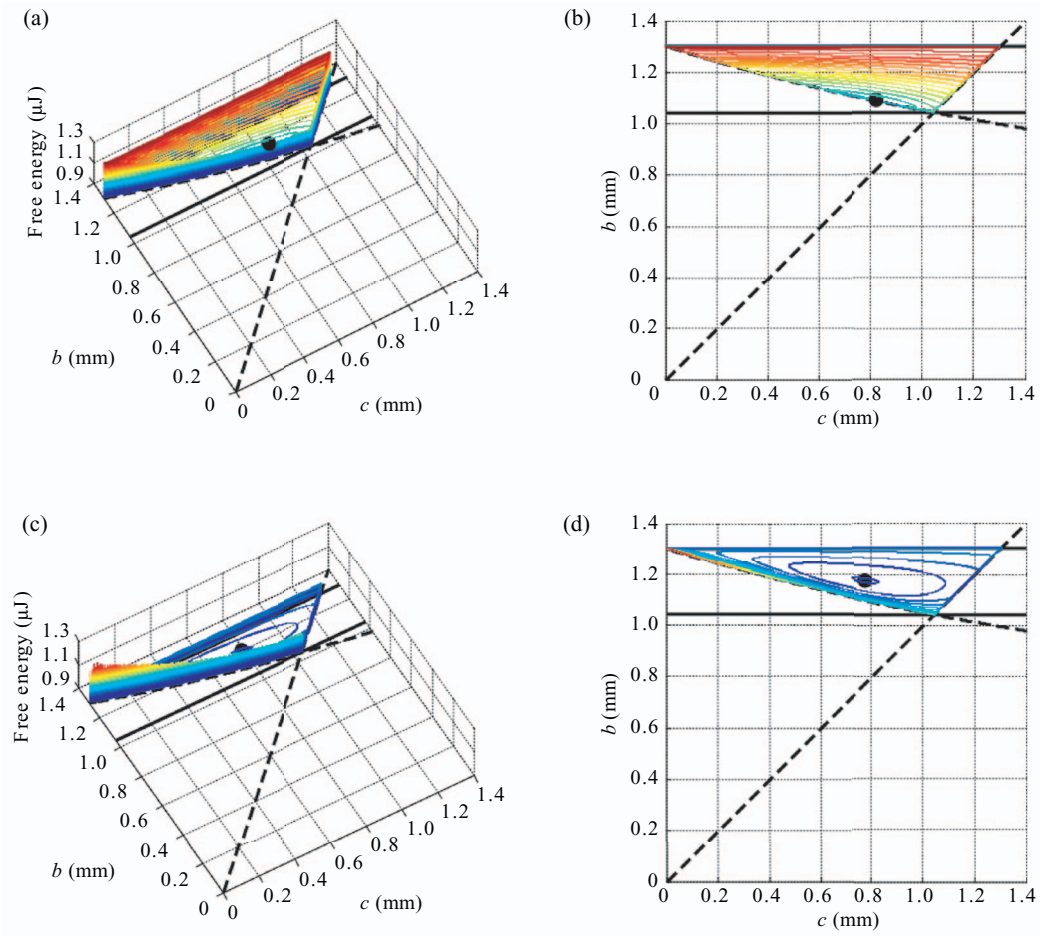

FIG. 5. The Gibbs free energy contour maps of a water drop with the volume of 5 μl. The Gibbs energy values of the drop on array II in (a) three-dimensional and (b) two-dimensional plots. The Gibbs energy values of the drop on the flat surface in (c) three-dimensional and (d) two-dimensional plots. The solid and dashed lines bound the range of b and c, respectively. The minimum free-energy point is denoted by a black dot.

caused by chemical heterogeneity, thermal or mechanical fluctuations. We suggest that this may be correlated with the contact angle hysteresis, but further study on this aspect is called for.

We compare the theoretical drop profiles with the actual drop images in Fig. 4. In the double-spheroid model, we try the values of k corresponding to the Wenzel and the Cassie-Baxter states for each rough surface. We also draw the profiles from the spherical-cap model which utilizes the drop volume and the experimentally measured apparent contact angle as input conditions. For the 5.0 μl drop on the flat hydrophobic surface, Fig. 4(a), the spherical-cap model differs little from the experimental image and the double-spheroid model. It is due to a small size of the drop (R_N = 1.1 mm) compared to l_c = 2.7 mm. However, as the drop size increases, the drop flattens as compared to the spherical cap shape, which is correctly predicted by our double-spheroid model. In Fig. 4(b), we compare the images of drops on array I with the spherical-cap model and the double-spheroid model assuming the Cassie-Baxter state ($k = 0.98$) in the left-half plane and with the double-spheroid model assuming the Wenzel state ($k = 0.52$) in the right-half plane. Except for the smallest drop (5 μl in volume), the models in the left-half plane exhibit considerable difference from the experiments. Our double-spheroid model assuming the Wenzel state agrees fairly well with experiments. On arrays II and III, whose results are shown in Figs. 4(c) and 4(d), respectively, the experimental drop shapes are compared with the spherical-cap model and the double-spheroid model assuming the Wenzel state ($k = 0.47$ and 0.54 for array II and III, respectively) in the left-half planes and with the double-spheroid model assuming the Cassie-Baxter state (k= 0.94 and 0.87

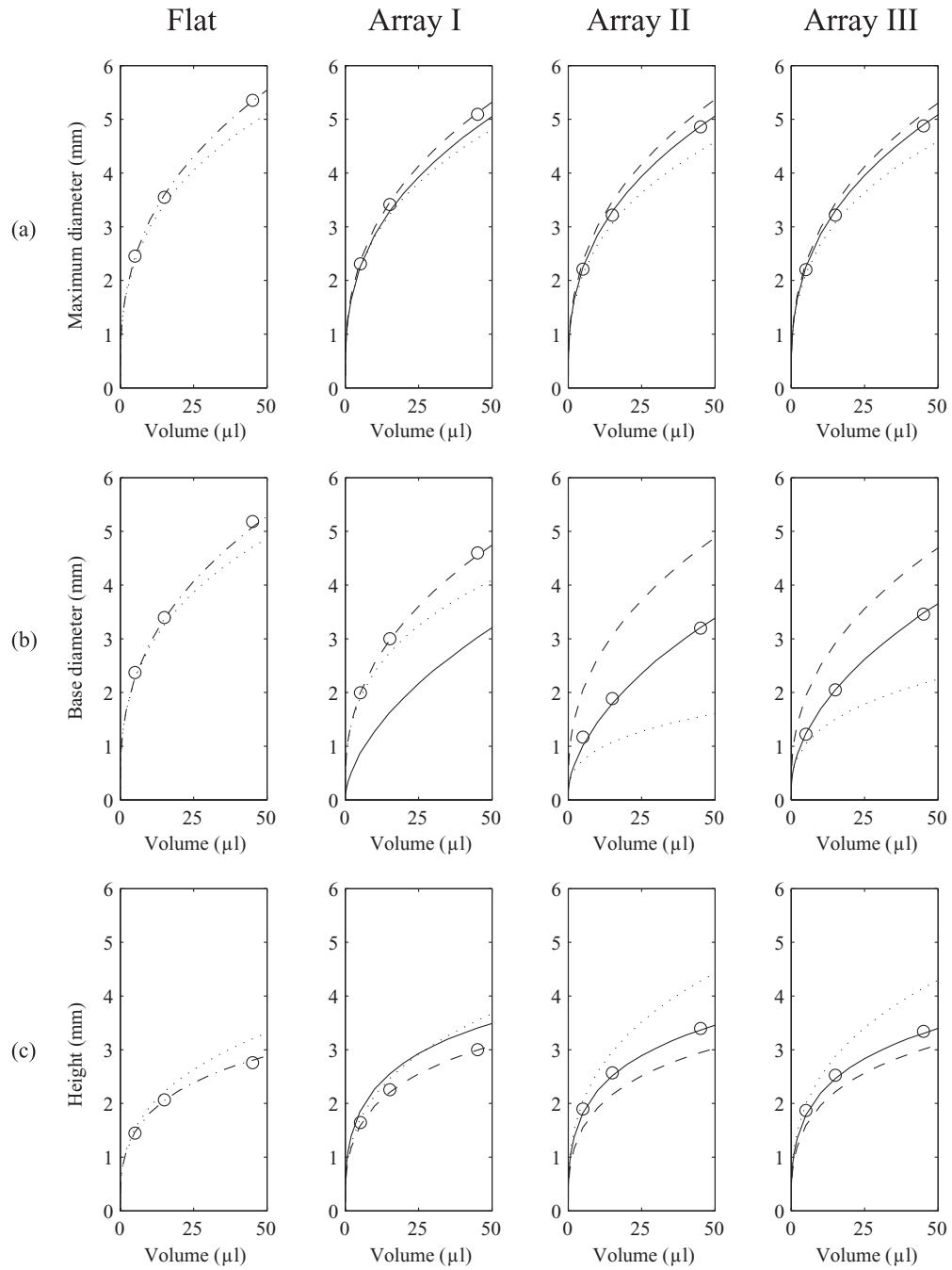

FIG. 6. Representative dimensions of the drops versus volume. (a) Maximum diameter; (b) base diameter; (c) height. The dotted line corresponds to the spherical-cap model, the dashed line to the double-spheroid model of the Wenzel state, the solid line to the double-spheroid model of the Cassie-Baxter state, and the dot-and-dash line to the double-spheroid model of the flat surface. The circles denote the experimental results.

for array II and III, respectively) in the right-half planes. In these cases, the double-spheroid model using the Cassie-Baxter state agrees well with experiment. These results illustrate the accuracy of our double-spheroid model in predicting the shape of gravitationally flattened large drops on rough hydrophobic surfaces. Also, we find that our theory can be used to deduce the wetting state of a large drop on rough surfaces by matching its actual shape with theoretically predicted profiles.

In Fig. 6, we compare the measured dimensions of the drops, i.e., maximum diameter ($2a$), base diameter ($2r_0$), and height ($b + z_0$), with the theoretical values. On the flat surfaces, the maximum

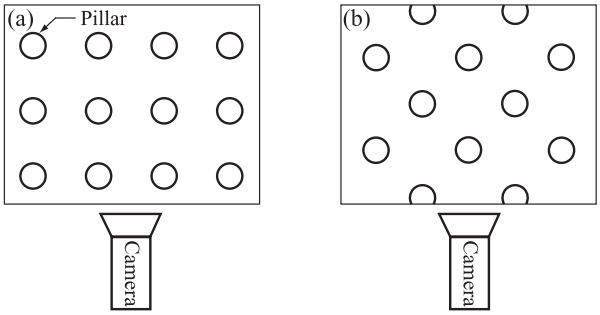

FIG. 7. Viewing angle with respect to the pillar lattice. (a) 0°; (b) 45°.

and base diameters are underestimated and the height is overestimated by the spherical-cap model, while the double-spheroid model accurately predicts each length. For micropillar arrays, the double-spheroid model of the Wenzel state predicts the largest maximum and base diameters and the smallest height among the models. The experimental measurements of array I are in good agreement with the double-spheroid model of the Wenzel state. The base and maximum diameters predicted by the double-spheroid model of the Cassie-Baxter state lie between the values predicted by the double-spheroid model of the Wenzel state and the spherical cap model. Also, the height of the Cassie-Baxter state is between the other two models except for small drops on array I. The experimental measurements of arrays II and III agree well with the double-spheroid model of the Cassie-Baxter state. The difference between the experimentally measured base diameter and the spherical-cap model increases with the drop volume, quantitatively indicating the gravitational flattening of the lower portion of the drop. In particular, such difference is greatly magnified in arrays II and III, revealing a higher sensitivity of the Cassie-Baxter drop's base area to gravitational flattening than the Wenzel drop's.

In the foregoing measurements, we used the lengths of drops as viewed at 0° with respect to the lattice of pillars (Fig. 7). Recently it was pointed out that the drop shape near the bottom can be asymmetrical when placed on micropillar arrays due to pinning of the contact line.[25] To quantify the effects of viewing angle on the length measurements, we measured the maximum and base diameters of water drops of the same range of volume as above on the three arrays viewed at 45° with respect to the lattice. The difference of maximum diameters of the drops of the same volume on the same array was below 1% for all the cases. The difference of the base diameters was the greatest for the smallest drops (5 μl in volume) and it grew as the pillar height increased. For drops of 5 μl volume on arrays I and III, the difference in the base diameter was 2.4% and 6.0%, respectively. For larger drops of 15 and 45 μl volume, the difference in the base diameter was at most 3.6% for all the arrays. These results are consistent with Papadopoulos *et al.*,[25] which reported that the drop profile becomes axisymmetric at a length scale 1 order of magnitude larger than the pillar height. Our comparison suggests that the drop asymmetry due to contact line pinning at micropillars (of maximum 40 μm height) hardly affects the maximum diameter values, which is measured at least 0.5 mm above the solid surface. The base diameter varies depending on the viewing angle within a limited range for small drops on tall pillar arrays. However, the drops having the nominal radius R_N much greater than the pillar height ($R_N = 1.5$ mm for a 15 μl-volume drop), the variation of the base diameter depending on the viewing angle is insignificant.

As mentioned above, the gravitational distortion becomes severe near the bottom of the drop, which leads us to adopt the double-spheroid model to account for the variation of the curvature along the z-direction. To quantify the degree of gravitationally induced flattening, we calculate the eccentricities e of the upper and lower ellipses for different conditions and show the results in Fig. 8. As e increases from 0, the ellipse deviates from being circular. The figure shows that within a single drop, the eccentricity of the lower spheroid is much greater than the upper one due to the effect of gravitational distortion. The eccentricity grows with the increase of the Bond number, defined as $\mathrm{Bo} = \rho g D^2/\gamma$ with D being the diameter of a sphere with the identical volume as the drop and the

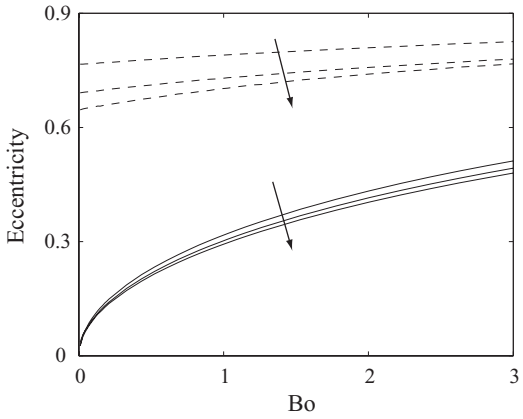

FIG. 8. Eccentricity of the upper (solid line) and lower (dashed line) ellipses as a function of Bo for varying k. k increases in the direction of the arrow taking the values 0.3, 0.6, and 0.9.

decrease of water repellency of the surface. While e of the upper spheroid increases from a very small value (less than 0.2) to about 0.5 with the increase of Bo, the lower spheroid exhibits a high eccentricity even at small drop volumes but its increase is not as steep as that of the upper spheroid. This signifies that even drops of small volumes can be locally flattened at the bottom, which is consistent with the previous experimental observations.[8]

The flattening of large drops can also be quantified by measuring the peak height ($b + z_0$) or the z-coordinate of the maximum diameter (i.e., equator height z_0) depending on drop size. Figure 9

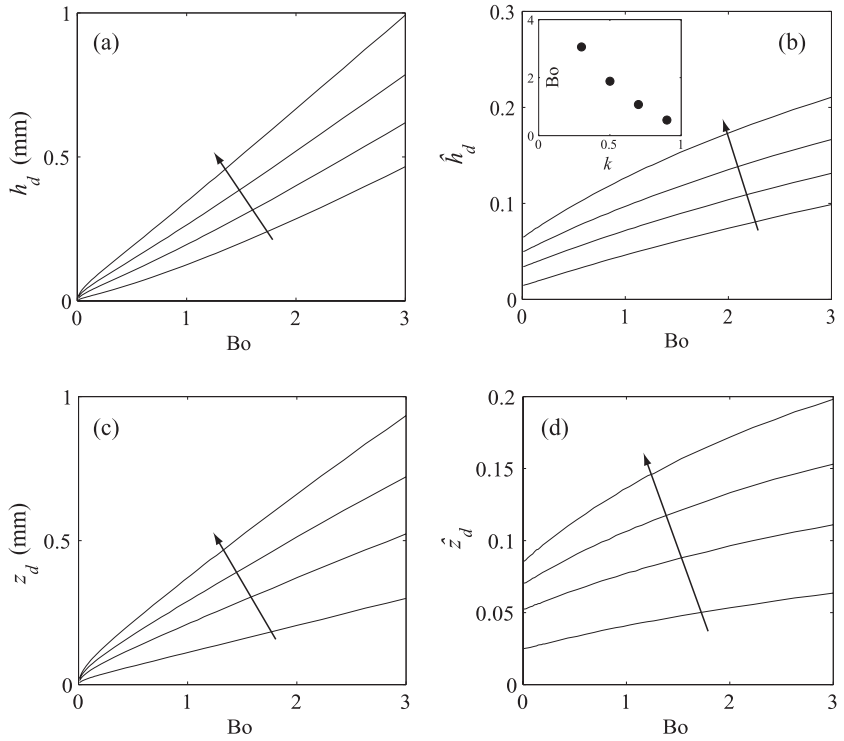

FIG. 9. Depressions of the peak and equator height versus Bo for different water repellency, quantified by k. (a) Dimensional peak height depression versus Bo; (b) dimensionless peak height depression $\hat{h}_d = h_d/D$ versus Bo. (Inset) The Bond number yielding $\hat{h}_d = 0.1$ versus k; (c) dimensional depression of the equator height $z_d = z_s - z_0$ versus Bo. (d) Dimensionless depression of the equator height $\hat{z}_d = z_d/V^{1/3}$ versus Bo. k increases in the direction of the arrow taking the values 0.3, 0.5, 0.7, and 0.9.

plots the decrease of peak height $h_d = h_s - (b + z_0)$ and the depression of equator height $z_d = z_s - z_0$ with h_s and z_s being the height of the apex and equator of the spherical cap with the contact angle $\theta = \cos^{-1}(-k)$, respectively. We also plot their values scaled by D, $\hat{h}_d = h_d/D$ and $\hat{z}_d = z_d/D$, versus Bo. We see that the depressions increase with the drop size (Bo) and the water repellency (k). On the surfaces of strong water repellency (e.g., $k = 0.9$), the depression of the peak and equator height exceeds 10% even before Bo reaches unity, revealing the non-negligible effect of gravity on small drops sitting on superhydrophobic surfaces. Our model allows us to predict the Bond number at which the peak height depression reaches 10% for different k, as displayed as the inset in Fig. 9(b). For drops on moderately hydrophobic surface (e.g., $k = 0.3$), the depression of peak height reaches 10% when the Bond number becomes 3, which corresponds to 4.71 mm in spherical drop diameter. At the same Bond number (Bo = 3), the depression reaches 21% on a surface with $k = 0.9$, again revealing the great influence of water repellency on drop height depression.

V. CONCLUSIONS

We have developed a novel model to describe the profile of a large drop on a rough hydrophobic surface using an overlapping geometry of double spheroids and the free energy minimization principle. While the Bashforth-Adams model that directly solves the Young-Laplace equation needs a contact angle to close the mathematical formulation to find the drop profile of a given volume, our model utilizes the wetting state that gives the interfacial free energy. Our model is advantageous in that one can predict the drop shape without measuring the actual contact angle, which is often harder than measuring the other linear dimensions of a drop, such as height and base diameter. Also, one can infer the wetting state of a large drop, without resorting to the apparent contact angle, by merely comparing measured linear dimensions of the drop with the predictions of our model. By comparing the drop profiles viewed at 0° and 45° with respect to the pillar lattice, the effects of asymmetry of the drop profile caused by contact line pinning on the linear dimensions are found to be insignificant for drops having sizes one or more orders of magnitude larger than the pillar height. The excellent agreement of our theory and experimental measurements has verified the capability of our model in predicting the shape and wetting state of large drops. Furthermore, the computational expense required in our model, which consists of algebraic equations, is much cheaper than the Bashforth-Adams model that solves the nonlinear partial differential equations. We point out that the apparent contact angle of drops placed on a solid surface can vary within a range when the contact angle hysteresis (CAH), i.e., the difference between the critical advancing and receding contact angles, is present although it has been ignored by most of the studies addressing the static shapes of sessile drops. Although such an effect is insignificant for superhydrophobic surfaces with a very low CAH, it is worth further study to investigate how the difference of the apparent and equilibrium contact angles affects the linear dimensions such as the height, base, and maximum diameters of large drops on rough hydrophobic surfaces. Finally we note that the topography of solid surface needs to be known *a priori* in our model to evaluate k. Thus the model is particularly useful in predicting shapes of large drops on artificially prepared surfaces with micro and nano-scale roughness, which are widely used in many technological areas including biochips,[26] adhesives,[27] sensors,[28] and actuators.[29]

ACKNOWLEDGMENTS

This work was supported by KIMM (Basic Research Program), Ministry of Knowledge Economy (Global Excellent Technology Innovation R&D Program), and National Research Foundation (Grant Nos. 2011-0030744 and 2012-008023) of Republic of Korea. H.Y.K. acknowledges the administrative support of SNU-IAMD.

[1] P. A. Durbin, "On the wind force needed to dislodge a drop adhered to a surface," J. Fluid Mech. **196**, 205 (1988).
[2] J. H. Moon, B. H. Kang, and H.-Y. Kim, "The lowest oscillation mode of a pendant drop," Phys. Fluids **18**, 021702 (2006).
[3] P. Dimitrakopoulos and J. J. L. Higdon, "On the gravitational displacement of three-dimensional fluid droplets from inclined solid surfaces," J. Fluid Mech. **395**, 181 (1999).

[4] H.-Y. Kim, H. J. Lee, and B. H. Kang, "Sliding of liquid drops down an inclined solid surface," J. Colloid Interface Sci. **247**, 372 (2002).
[5] T. Young, "An essay on the cohesion of fluids," Philos. Trans. R. Soc. London **95**, 65 (1805).
[6] P. S. Laplace, *Mecanique Celeste, Supplement to the Tenth Edition* (Courier, Paris, 1806).
[7] F. Bashforth and J. C. Adams, *An Attempt to Test the Theories of Capillary Action by Comparing the Theoretical and Measured Forms of Drops of Fluid* (Cambridge University Press, UK, 1883).
[8] C. W. Extrand and S. I. Moon, "Contact angles of liquid drops on super hydrophobic surfaces: Understanding the role of flattening of drops by gravity," Langmuir **26**, 17090 (2010).
[9] H. Y. Erbil and R. A. Meric, "Evaporation of sessile drops on polymer surfaces: Ellipsoidal cap geometry," J. Phys. Chem. B **101**, 6867 (1997).
[10] G. Whyman and E. Bormanshenko, "Oblate spheroid model for calculation of the shape and contact angles of heavy droplets," J. Colloid Interface Sci. **331**, 174 (2009).
[11] V. A. Lubarada and K. A. Talke, "Analysis of the equilibrium droplet shape based on an ellipsoidal droplet model," Langmuir **27**, 10705 (2011).
[12] E. Moy, P. Cheng, Z. Policova, S. Treppo, D. Kwok, D. P. Mack, P. M. Sherman, and A. W. Neumann, "Measurement of contact angles from the maximum diameter of non-wetting drops by means of a modified axisymmetric drop shape analysis," Colloids Surf. **58**, 215 (1991).
[13] P. Cheng and A. W. Neumann, "Computational evaluation of axisymmetric drop shape analysis-profile (ADSA-P)," Colloids Surf. **62**, 297 (1992).
[14] D. Y. Kwok, T. Gietzelt, K. Grundke, H.-J. Jacobasch, and A. W. Neumann, "Contact angle measurements and contact angle interpretation. 1. Contact angle measurements by axisymmetric drop shape analysis and a goniometer sessile drop technique," Langmuir **13**, 2880 (1997).
[15] R. N. Wenzel, "Resistance of solid surfaces to wetting by water," Ind. Eng. Chem. **28**, 988 (1936).
[16] A. B. D. Cassie and S. Baxter, "Wettability of porous surfaces," Trans. Faraday Soc. **40**, 546 (1944).
[17] L. Gao and T. J. McCarthy, "How Wenzel and Cassie were wrong," Langmuir **23**, 3762 (2007).
[18] A. W. Adamson and A. P. Gast, *Physical Chemistry of Surfaces*, 6th ed. (Wiley, New York, 1997).
[19] J. N. Israelachvili, *Intermolecular and Surface Forces*, 2nd ed. (Academic, London, 1992).
[20] G. Whyman, E. Bormashenko, and T. Stein, "The rigorous derivation of Young, Cassie-Baxter and Wenzel equations and the analysis of the contact angle hysteresis phenomenon," Chem. Phys. Lett. **450**, 355 (2008).
[21] R. Tadmor and R. S. Yadav, "As-placed contact angles for sessile drops," J. Colloid Interface Sci. **317**, 241 (2008).
[22] E. Hernández-Baltazar and J. Gracia-Fadrique, "Elliptic solution to the Young-Laplace differential equation," J. Colloid Interface Sci. **287**, 213 (2005).
[23] A. Hozumi, K. Ushiyama, H. Sugimura, and O. Takai, "Fluoroalkylsilane monolayers formed by chemical vapor surface modification on hydroxylated oxide surfaces," Langmuir **15**, 7600 (1999).
[24] M. Reyssat, J. M. Yeomans, and D. Quéré, "Impalement of fakir drops," Europhys. Lett. **81**, 26006 (2008).
[25] P. Papadopoulos, X. Deng, L. Mammen, D.-M. Drotlef, G. Battagliarin, C. Li, K. Müllen, K. Landfester, A. del Campo, H.-J. Butt, and D. Vollmer, "Wetting on the microscale: Shape of a liquid drop on a microstructured surface at different length scales," Langmuir **28**, 8392 (2012).
[26] H.-Y. Li, V. Dauriac, V. Thibert, H. Senechal, G. Peltre, X.-X. Zhang, and S. Descroix, "Micropillar array chips toward new immunodiagnosis," Lab Chip **10**, 2597 (2010).
[27] E. Cheung and M. Sitti, "Adhesion of biologically inspired oil-coated polymer micropillars," J. Adhes. Sci. Technol. **22**, 569 (2008).
[28] S. Große, W. Schröder, and C. Brücker, "Nano-newton drag sensor based on flexible micro-pillars," Meas. Sci. Technol. **17**, 2689 (2006).
[29] Y. Akiyama, K. Iwabuchi, Y. Furukawa, and K. Morishima, "Long-term and room temperature operable bioactuator powered by insect dorsal vessel tissue," Lab Chip **9**, 140 (2009).